J. Fluid Mech. (2026), *vol.* 1030, R3, doi:10.1017/jfm.2026.11262

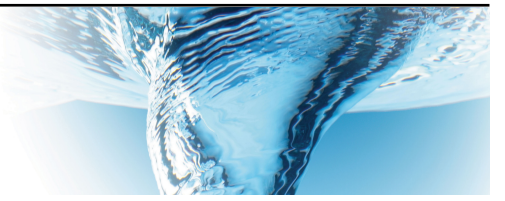

Wave attenuation in drifting sea ice: a mechanistic model for observed decay profiles

Rhys Ransome[1], **Davide Proment**[1,2,3], **Ian Renfrew**[4] and **Alberto Alberello**[1]

[1]School of Mathematics, University of East Anglia, Norwich Research Park, Norwich NR4 7TJ, UK

[2]Centre for Photonics and Quantum Science, University of East Anglia, Norwich Research Park, Norwich NR4 7TJ, UK

[3]ExtreMe Matter Institute EMMI, GSI Helmholtzzentrum fuer Schwerionenforschung, Planckstrasse 1, 64291 Darmstadt, Germany

[4]School of Environmental Sciences, University of East Anglia, Norwich Research Park, Norwich NR4 7TJ, UK

Corresponding author: Rhys Ransome, R.Ransome@uea.ac.uk

(Received 28 October 2025; revised 27 January 2026; accepted 27 January 2026)

Wave–sea-ice interactions shape the transition zone between open ocean and pack ice in the polar regions. Most theoretical paradigms, implemented in coupled wave–sea-ice models, predict exponential decay of the wave energy but some recent observations deviate from this behaviour. Expanding on a framework based on wave energy dissipation due to ice–water drag, we account for drifting sea ice to derive an improved model for wave energy attenuation. Analytical solutions replicate the observed non-exponential wave energy decay and the spatial evolution of the effective attenuation rate in Antarctic sea ice.

Key words: surface gravity waves, sea ice, wave-structure interactions

1. Introduction

Sea ice that seasonally forms in the polar regions regulates heat and momentum fluxes between the ocean and the atmosphere over large scales, thereby playing a crucial role in the global weather and climate system (e.g. IPCC 2021; Bennetts *et al.* 2024; Selivanova, Iovino & Cocetta 2024). The transition zone between the open ocean and the pack ice, often referred to as the marginal ice zone (MIZ; Wadhams 1986), is the most dynamic, yet poorly understood, component of such system (Landwehr *et al.* 2021; Vichi 2022; Day *et al.* 2024).

The interaction of ocean waves propagating into the sea ice is a defining feature of the Arctic and Antarctic MIZ (Kohout *et al.* 2014; Stopa, Sutherland & Ardhuin 2018; Alberello *et al.* 2022; Brouwer *et al.* 2022; Day *et al.* 2024), and in the Southern Ocean this region extends for hundreds of kilometres. Wave energy decays with distance into the MIZ, with the attenuation rate α, i.e. $E(x) \propto \exp(-\alpha x)$, assumed to be proportional to the wave frequency f to some power ($\alpha \propto f^p$; e.g. Meylan *et al.* 2018). The exact frequency dependency varies according to the dominant attenuation mechanism, and various options are implemented in operational third generation spectral wave models (e.g. WaveWatchIII; Montiel *et al.* 2025) that are being coupled into global- and hemispheric-scale ocean–sea-ice models. Most models predict a constant attenuation rate in homogeneous sea-ice conditions and, consequently, exponential wave energy decay.

Overall, measurements conform reasonably well to the exponential attenuation paradigm and agree on the magnitude of the attenuation rate α, within the range (10^{-4} $\mathrm{m}^{-1} < \alpha < 10^{-5}$ m^{-1}; Kohout *et al.* 2020; Montiel, Kohout & Roach 2022). However, recent satellite measurements of wave height in the Antarctic MIZ across seasons revealed an almost linear increase of the average attenuation rate with distance from the sea-ice edge (up to $\approx 10\times$; Voermans *et al.* 2025) with individual transects showing sharp peaks in attenuation rate. Possible causes of deviation from the exponential profile were attributed to the misalignment between the transect and wave direction, and inhomogeneous sea-ice conditions (sea-ice concentration and thickness). Lacking a firm theoretical foundation, Voermans *et al.* (2025) propose an empirical wave attenuation formulation as an interim solution for implementation in wave models, i.e. $\alpha = \beta x / x_{MIZ} - \gamma$ in which β and γ are empirical fitting parameters and x_{MIZ} is the extent of the MIZ. The formulation leads to exponential energy decay at a rate βx^2.

Amongst the various theoretical wave attenuation models, the ones that attribute wave energy dissipation to quadratic ice–water drag deviate from exponential decay in form. Ice–water drag models capture the bulk of the energy loss when sea ice comprises floes with small diameter, relative to wavelength, in high concentration (Shen & Squire 1998; Kohout, Meylan & Plew 2011; Herman, Cheng & Shen 2019) as further supported by experimental observations (Smith & Thomson 2020). This makes these models well suited to the Antarctic MIZ. The attenuation rate due to drag is proportional to the square of the relative velocity between fluid orbital motion and sea ice (Herman *et al.* 2019). Assuming a stationary semi-infinite sea-ice domain, analytical, non-exponential, solutions for the amplitude profile have been obtained under slightly different approaches by Kohout *et al.* (2011), for the amplitude envelope, and Herman *et al.* (2019), for the phase-averaged amplitude. The former is a lower bound for the amplitude, i.e. a higher bound for the attenuation rate.

The drift of sea ice is a feature of the MIZ dynamics throughout the year (Kwok, Pang & Kacimi 2017; Day *et al.* 2024). The Southern Ocean, under persistent waves (Derkani *et al.* 2020), is characterised by unconsolidated small floes ($\approx$10 m in diameter) in high concentration (>80 %; Alberello *et al.* 2019; Day *et al.* 2024) with little internal stresses (Alberello *et al.* 2020; Womack *et al.* 2022). In these conditions, wind is the main driver of sea-ice drift (Holland & Kwok 2012; Kwok *et al.* 2017). Through air–ice drag coefficients of order 10^{-3} (Wamser & Martinson 1993; Elvidge *et al.* 2016), sea ice drifts at 0.1–0.4 m s^{-1} with low variability over large scales (10–100 km; Holland & Kwok 2012). Nevertheless, the drift of the MIZ is particularly intense during extreme events when concurrent energetic ocean wave are able to penetrate hundreds of kilometres into the sea ice, as demonstrated by recent observations (Vichi *et al.* 2019; Alberello *et al.* 2020; Womack *et al.* 2022, 2024). These events are likely the main contributors to the overall

MIZ dynamics. However, to the best of our knowledge, the interplay between drift and wave attenuation has not been explored before.

Several of the world's leading meteorological agencies have moved to using coupled atmosphere–ocean–sea-ice forecasting systems in the last few years to improve forecasting of near-surface temperature, humidity, winds and low-level clouds, as well as sea-ice distribution in the polar regions. In this regard, prediction in the MIZ is proving a particularly difficult challenge (Day *et al.* 2022; Barrell *et al.* 2025). One aspect of focussed development is the coupling of physics-based ocean wave and sea-ice models within a dynamical ocean model, so subject to drift (Kousal *et al.* 2026), making this study timely with the potential to inform this development.

Here, we develop a new analytical framework for the attenuation of monochromatic waves due to drag, explicitly accounting for constant sea-ice drift.

We extend the previous works of Kohout *et al.* (2011) and Herman *et al.* (2019) where drift was neglected on the grounds that, in typical oceanic conditions, drift velocities are two orders of magnitude smaller than the wave group velocity. Despite its apparently negligible effect, we reveal distinctive consequences of including such drift, most notably the emergence of a location into the ice field where the wave amplitude vanishes and the attenuation rate becomes unbounded. We further demonstrate the capability of this enhanced model to reproduce recent observations of wave attenuation in the Antarctic MIZ.

2. Mathematical formulation and analytical solutions

The one-dimensional wave energy transport equation for energy density per unit surface area, $E(x, t)$, in sea-ice-covered regions and excluding all other source terms is

$$\frac{\partial E}{\partial t} + c_g \frac{\partial E}{\partial x} = S_{ice} = S_{sd} + S_{exp}, \tag{2.1}$$

where c_g denotes the group velocity and, similarly to Kohout *et al.* (2011), the effect of the ice (S_{ice}) is explicitly expressed as a linear superposition of all the mechanisms with constant decay, that lead to exponential attenuation (S_{exp}), and the ones due to ocean–ice skin drag (S_{sd}). Note that the assumption of exponential decay for all the mechanisms other than drag will facilitate analytic handling. Here, in agreement with most wave-in-ice parametrisations in WaveWatchIII (Montiel *et al.* 2025), we assume the open water dispersion relation between angular frequency ω and wavenumber k to hold in sea ice.

The transport equation in terms of wave amplitude $a(x, t)$, using $E = \frac{1}{2}\rho g a^2$, where ρ is water density and g acceleration due to gravity, becomes

$$a\frac{\partial a}{\partial t} + a c_g \frac{\partial a}{\partial x} = s_{ice} = s_{exp} + s_{sd}, \tag{2.2}$$

where $s = S/\rho g$. In agreement with previous work (e.g. Kohout *et al.* 2011; Herman *et al.* 2019), in ice-covered regions we define the exponential source term as

$$s_{exp} = -c_g \alpha_{exp} a^2, \tag{2.3}$$

where α_{exp} is the constant amplitude attenuation rate for all other contributing non-skin-drag mechanisms e.g. wave scattering (Wadhams 1978), viscous dissipation (Weber 1987; Keller 1998) and visco-elasticity (Robinson & Palmer 1990; Fox & Squire 1994; Wang & Shen 2010). Its inclusion provides flexibility for future operational model implementations.

In ice-covered regions, for a monochromatic wave, the skin-drag stress at the ice–ocean interface follows a standard quadratic law, $\tau = \rho C_d |u_{orb} - v|(u_{orb} - v)$ (Shen & Squire

1998), with C_d the drag coefficient. The rate of change of energy per unit area due to skin drag is proportional to $|u_{orb} - v|^3$ (Shen & Squire 1998), where $u_{orb} = U \sin(\phi)$ is the wave orbital velocity at the ice–water interface, here evaluated at the free surface under the hypothesis of thin sea ice, and v is the ice drift velocity. The magnitude of the orbital velocity is $U = a\Omega$, where $\Omega = gk/\omega$, and ϕ is time-dependent phase. Phase averaging, we obtain

$$s_{sd} = -\frac{C_d}{g}\frac{1}{2\pi}\int_0^{2\pi} |a\Omega \sin(\phi) - v|^3 \, \mathrm{d}\phi. \tag{2.4}$$

We consider a thin semi-infinite homogenised sea-ice layer drifting at a constant velocity v and arbitrarily set a frame of reference moving at v, i.e. $\hat{x} = x - vt$, with $\hat{x}$ the distance from the edge of the sea ice. Taking the steady-state system in the moving frame with a constant wave forcing at the ice edge $a(0) = a_0$, the one-dimensional wave energy transport equation (2.2) in the ice region ($\hat{x} \geqslant 0$) reduces to

$$\frac{\mathrm{d}a}{\mathrm{d}\hat{x}} = -\alpha\, a - \frac{\Gamma}{a}\int_0^{2\pi} |a\Omega \sin(\phi) - v|^3 \, \mathrm{d}\phi\,, \tag{2.5}$$

with

$$\Gamma = \frac{C_d}{2\pi g (c_g - v)}\,, \quad \text{and} \quad \alpha = \frac{c_g}{c_g - v}\alpha_{exp}, \tag{2.6}$$

being the attenuation, therefore remaining exponential in the moving frame.

2.1. *Solving the amplitude profile*

Equation (2.5) represents a challenging nonlinear ordinary differential equation. Here, we aim to derive an analytical solution and to facilitate the mathematical treatment we assume the parameters C_d and α to be spatially homogeneous (constant). The model can be extended for heterogeneous conditions but numerical solutions should be sought. A polynomial in a for the integral of the skin drag (2.4) can be found explicitly in closed form for $|v| \geqslant a\Omega$, see Appendix A. In effort to enable closed form analytical solutions we seek an approximate polynomial form using an asymptotic expansion of the integrand for $|v| \ll a\Omega$ that is then extended into the region $|v| < a\Omega$ (see Appendix A). We obtain

$$I = \int_0^{2\pi} |a\Omega \sin(\phi) - v|^3 \mathrm{d}\phi \begin{cases} \approx \dfrac{8}{3}(a\Omega)^3 + 12a\Omega v^2, & \text{if } |v| < a\Omega; \\ = 3\pi(a\Omega)^2|v| + 2\pi|v|^3, & \text{if } |v| \geqslant a\Omega. \end{cases} \tag{2.7}$$

Note that, in oceanic conditions, c_g is two orders of magnitude lager than the wind- and current-induced drift, i.e. $\mathcal{O}(10)\ \mathrm{m\,s^{-1}}$ versus $\mathcal{O}(0.1)\ \mathrm{m\,s^{-1}}$, therefore $|v| \ll c_g$ implying that, with α and Γ positive, (2.7) is strictly positive, therefore the amplitude a decreases monotonically in (2.5). For $a_0\Omega > |v|$, we define $\hat{x}^*$ to be the location into the ice domain such that $a(\hat{x}^*)\Omega = |v|$. Therefore, the condition $|v| \lessgtr a\Omega$ corresponds to $\hat{x} \lessgtr \hat{x}^*$ in the physical domain. In contrast, for $a_0\Omega \leqslant |v|$, one obtains $\hat{x}^* = 0$.

Solving (2.5) with the integral approximation (2.7), the amplitude solutions are written in piecewise form as

$$a(\hat{x}) \approx a_A(\hat{x})\, \mathbf{1}_{\{\hat{x} < \hat{x}^*\}} + a_B(\hat{x})\, \mathbf{1}_{\{\hat{x} \geqslant \hat{x}^*\}}, \tag{2.8}$$

where $\mathbf{1}$ is the indicator function, equal to 1 if the condition is true and 0 otherwise. The piecewise solution components result in

$$a_A(\hat{x}) = \begin{cases} \dfrac{3\sqrt{\Delta}}{16\Gamma\Omega^3}\tan\left(-\dfrac{\sqrt{\Delta}}{2}\hat{x} + \arctan\left(\dfrac{16\Gamma\Omega^3 a_0 + 3\alpha}{3\sqrt{\Delta}}\right)\right) - \dfrac{3\alpha}{16\Gamma\Omega^3}, & \delta > 1, \\ \dfrac{32\Gamma\Omega^3 a_0 - \left(16\alpha\Gamma\Omega^3 a_0 + 3\alpha^2\right)\hat{x}}{32\Gamma\Omega^3 + \left(32\Gamma\Omega^3 a_0 + 6\alpha\right)\hat{x}}, & \delta = 1, \\ \dfrac{r_-(a_0 - r_+)\exp\left(\dfrac{8\Gamma\Omega^3}{3}(r_- - r_+)\hat{x}\right) - r_+(a_0 - r_-)}{(a_0 - r_+)\exp\left(\dfrac{8\Gamma\Omega^3}{3}(r_- - r_+)\hat{x}\right) - (a_0 - r_-)}, & \delta < 1, \end{cases} \tag{2.9}$$

$$a_B(\hat{x}) = \left[e^{-(6\pi\Omega^2|v|\Gamma + 2\alpha)(\hat{x} - \hat{x}^*)}\left(\frac{v^2}{\Omega^2} + \frac{2\pi|v|^3\Gamma}{3\pi\Omega^2|v|\Gamma + \alpha}\right) - \frac{2\pi|v|^3\Gamma}{3\pi\Omega^2|v|\Gamma + \alpha}\right]^{\frac{1}{2}}. \tag{2.10}$$

Here, $\Delta \equiv \alpha^2(\delta^2 - 1)$, $r_\pm \equiv -3(\alpha \pm \sqrt{-\Delta})/(16\Gamma\Omega^3)$ and

$$\delta = \frac{8\sqrt{2}\Gamma\Omega^2|v|}{\alpha}, \tag{2.11}$$

which controls the roots of the quadratic polynomial in a affecting the solution in the $\hat{x} < \hat{x}^*$ region (see Appendix B). Note that the physical interpretation of δ will be discussed in § 2.2.

The solution has a few interesting features. The amplitude profile is continuous in $\hat{x}$ (see Appendix B). The solution is nonlinear, i.e. drag effects and other mechanisms cannot be added as linear superposition. For $\hat{x} < \hat{x}^*$, the different branches of the solution in (2.9) differ in form but possess similar qualitative behaviour, where we note that $\hat{x}^*$ depends on δ. For a wave with initial orbital velocity magnitude $U_0 < |v|$ we obtain the solution in region B, a_B, applies to the entire domain $\hat{x} \geqslant 0$.

A distinctive consequence of such solution is the existence of an extinction location

$$\hat{x}_{end} = \hat{x}^* + \frac{8}{3\sqrt{2}\pi\alpha\delta + 8}\log\left(\frac{5}{2} + \frac{4\sqrt{2}}{\pi\delta}\right), \tag{2.12}$$

such that $a_B(\hat{x} = \hat{x}_{end}) = 0$. The extinction location is always in region B because it is where amplitude tends to zero and the condition $a\Omega < |v|$ is satisfied. The extinction location is unique to dissipation due to drift-induced skin drag and defines the extent of the wave-affected region. It moves closer to the sea-ice edge for increasing C_D coefficient and α, see solution in red, for $v = 0.05$ m s^{-1} and $\alpha = 7 \times 10^{-6}$ m^{-1} ($\delta = 3.4$), vs in blue, for $v = 0.05$ m s^{-1} and $\alpha = 0$ ($\delta = \infty$), in figure 1(*a*), while its dependence on drift is not trivial. Such extinction locations are not present in the solutions of Kohout *et al.* (2011) and Herman *et al.* (2019), shown in dashed green and orange respectively in figure 1*a*), for which $\alpha = 0$ and $v = 0$.

In the special case of no drift, i.e. $v = 0$, the solution reduces to

$$a(\hat{x}) = \frac{3a_0\alpha e^{-\alpha\hat{x}}}{3\alpha + 8a_0\Gamma\Omega^3 - 8a_0\Gamma\Omega^3 e^{-\alpha\hat{x}}}. \tag{2.13}$$

Taking $C_d = 0$, i.e. no drag, we recover the exponential attenuation at a rate α, whereas for $\alpha \to 0$, the solution converges to the one of Herman *et al.* (2019). Therefore, (2.13) is an extension Herman *et al.* (2019) that accounts for additional mechanisms. As a result, our solution predicts lower amplitudes compared with Herman *et al.* (2019), see figure 1(*a*).

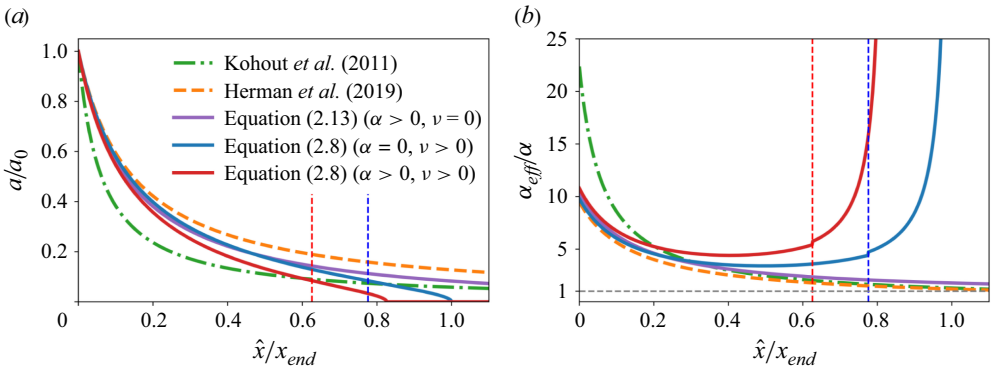

Figure 1. Sample amplitude (a) and corresponding attenuation (b) profiles according to our model and formulations by Kohout *et al.* (2011) and Herman *et al.* (2019). Dashed lines denote x^*, which denotes the separation between regions A and B. Amplitude is normalised by the initial amplitude and distance by x_{end} for $\alpha = 0$. Attenuation rate is normalised by α. Solutions are shown for $a_0 = 1$ m, $C_d = 0.05$, $v = 0.053\ \mathrm{m\,s^{-1}}$, $\omega = 0.63\ \mathrm{s^{-1}}$, $\alpha = 7.2 \times 10^{-6}\ \mathrm{m^{-1}}$.

Figure 1(a) displays the normalised amplitude as a function of the distance into the MIZ normalised by the value x_{end} computed for the non-zero drift and exponential attenuation case ($v = 0.053\ \mathrm{m\,s^{-1}}$ and $\alpha = 0$; the case displayed in blue). The attenuation is stronger when drift is present, as shown in red ($v > 0$ and $\alpha = 7 \times 10^{-6}$), compared with the solution in purple with $v = 0\ \mathrm{m\,s^{-1}}$ and $\alpha = 7 \times 10^{-6}$. The increased attenuation due to other mechanisms also manifests when drift is present, see solutions in blue vs in red.

2.2. *Predicting the attenuation rate*

To allow for better comparison with attenuation results for non-drifting sea ice as they appear in the literature (Kohout *et al.* 2011; Herman *et al.* 2019) and to better highlight the attenuation characteristics, we compute the effective amplitude attenuation rate in the moving frame in the ice-covered region defined as

$$\alpha_{eff} \equiv -\frac{1}{a}\frac{\mathrm{d}a}{\mathrm{d}\hat{x}} = \alpha + \frac{\Gamma}{a^2} I\,. \tag{2.14}$$

Using the integral estimation (2.7) we obtain

$$\alpha_{eff}(\hat{x}) \begin{cases} \approx \alpha + \dfrac{8}{3} a \Omega^3 \Gamma + \dfrac{12 \Omega v^2 \Gamma}{a}, & \text{if } \hat{x} < \hat{x}^*; \\ = \alpha + 3\pi \Omega^2 |v| \Gamma + \dfrac{2\pi |v|^3 \Gamma}{a^2}, & \text{if } \hat{x} \geqslant \hat{x}^*. \end{cases} \tag{2.15}$$

Note that, by extending asymptotic solution of I for $|v| < a\Omega$ to $|v| = a\Omega$, the decay rate inherits a jump discontinuity at $\hat{x}^*$, shown in figure 1(b), with the suitability of the integral approximation justified by the discontinuity magnitude being only 7 %. The nonlinearity between skin drag and other exponential decay mechanisms leads to the lower bound

$$\alpha_{eff} \geqslant \alpha + 8\sqrt{2}\Gamma\Omega^2|v| = \alpha(1 + \delta)\,, \tag{2.16}$$

with the global minimum located in the region $\hat{x} < \hat{x}^*$ if $a_0\Omega \geqslant 3\sqrt{2}|v|/2$, whereas for lower orbital velocity at the sea-ice edge the attenuation monotonically increases. This result allows for a physical interpretation of the dimensionless parameter δ: for $\delta > 1$ wave

attenuation is dominated by drift-induced skin drag and for $\delta < 1$ all other mechanisms dominate.

For drifting sea ice, the attenuation rate grows unbounded in the neighbourhood of the extinction location (see solutions in red and blue in figure 1(*b*)), i.e. $\alpha_{eff}(\hat{x}) \sim [2(x_{end} - \hat{x})]^{-1}$, therefore the extinction location affects the magnitude of the attenuation rate in this region. When drift is absent, $\hat{x}^* \to \infty$ and the solution for $\hat{x} < \hat{x}^*$ applies to the entire domain. As a consequence of our model, skin drag dominates attenuation close to the sea-ice edge whereas other processes dominate deeper into the sea ice, where we retrieve the classical exponential attenuation, i.e. $\alpha_{eff} \to \alpha$ for $\hat{x} \to \infty$ (see solution in purple in figure 1(*b*); the grey dashed line denotes $\alpha_{eff} = \alpha$).

3. Comparisons with Antarctic measurements

In this section comparisons are made with measured amplitudes and derived attenuations in the Antarctic sea ice (Brouwer *et al.* 2022; Voermans *et al.* 2025). The observations comprise quality controlled ICESat-2 satellite transects of wave height (both the total wave heights and the spectral wave heights corresponding to frequency bands at periods $T = 9$, 12, 15, 18 s) across the MIZ throughout 2019. Note that transects seldom start at the ice edge (possibly because they fail quality control at intermediate sea-ice concentrations) and, in computing attenuation rates, transects are assumed to align with the wave direction (Voermans *et al.* 2025). Drift is not measured by ICESat-2.

To compare observations with model results, which are derived for a monochromatic wave, we attribute all energy to the most energetic frequency component measured over the transect, normalising amplitude and attenuation rate by the first available measurement from the ice edge, a_V^1 and α_V^1. The ice edge is taken to coincide be the start of each transect. To allow for a straightforward comparison of the model with the observations we use x in place of $\hat{x}$, noting that their difference is negligible for small drift velocities. Moreover, in agreement with the observations, transects are normalised by MIZ extent x_{MIZ}. In this regard it is important to note that the MIZ extent is reported independently from the wave amplitude, i.e. low-amplitude readings were excluded due to quality control (Voermans *et al.* 2025).

Drift and drag are used as fitting parameters, within the range of available Antarctic sea-ice observations, i.e. $v = \mathcal{O}(10^{-1})$ m s^{-1} and $C_d = \mathcal{O}(10^{-2})$, together with α. While least squares optimisation was attempted, the noise in the observational data prevented reasonable fitting throughout the transect. For illustrative purposes, we performed manual tuning for each transect of the parameters within ranges of characteristic values for the MIZ. The drift is assumed to be constant along the transect, justified by slow spatial variation over 10–100 km in Antarctic sea ice (Holland & Kwok 2012). The water density is set to $\rho = 1025$ kg m^{-3} and the deep water dispersion relation is used, namely $\Omega = \omega$.

3.1. *Individual transects*

The two transects reported in Voermans *et al.* (2025) are analysed in detail. Transect I, taken on 26 December 2019 at 85°W, 69°S, is 61.5 km long and waves have a peak period of 15 s with amplitude $a_V^1 = 0.45$ m and attenuation, $\alpha_V^1 = 1.42 \times 10^{-5}$ m^{-1}. Transect II, taken on 24 May 2019 at 88°W, 68°S, is longer ($x_{MIZ} = 137.5$ km) and waves have a shorter peak period ($T = 12$ s) with amplitude $a_V^1 = 0.55$ m and attenuation, $\alpha_V^1 = 2.43 \times 10^{-6}$ m^{-1}.

For transect I the parameters $v = 0.26$ m s^{-1}, $C_d = 6.0 \times 10^{-3}$ and $\alpha = 5.0 \times 10^{-6}$ provide good qualitative and quantitative agreement in terms of amplitude decay

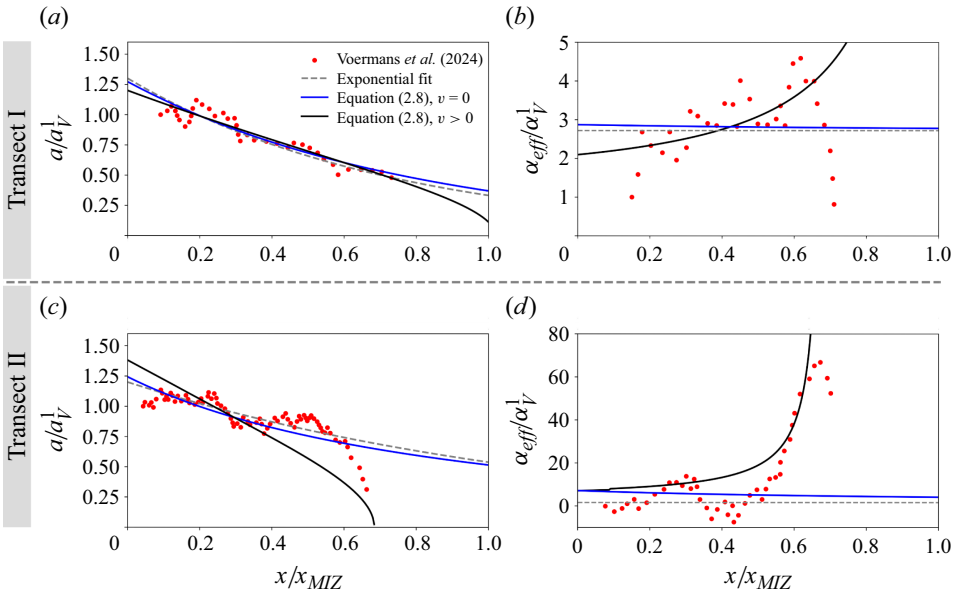

Figure 2. Amplitude (*a*,*c*) and corresponding attenuation profiles (*b*,*d*) for transects A (top) and B (bottom). Measurements (red dots) are shown against model predictions. Distance is normalised with respect to the wave-affected sea-ice extent x_{MIZ} and amplitude/attenuation with respect to the measurement closest to the sea-ice edge as reported in Voermans *et al.* (2025).

(see figure 2(*a*)). Similar performances are achieved by the the non-drifting model, i.e. $v = 0$, and the exponential decay. However, the model with drift outperforms the others, reproducing the observed increase in effective attenuation rate along the transect (between $x/x_{MIZ} \approx 0.2$ and 0.6; see figure 2(*b*)). Note that, for the chosen parameters, drift is stronger than the orbital velocity throughout the transect ($|v|/U_0 \approx 1.2$), i.e. only the branch $x > \hat{x}^*$ of (2.15) is used. Remarkably, the model predicts an extinction location consistent with the observed wave-affected sea-ice extent, i.e. at $x/x_{MIZ} \approx 1$.

For transect II the parameters $v = 0.49$ m s^{-1}, $C_d = 2.8 \times 10^{-3}$ and $\alpha = 1.0 \times 10^{-7}$ qualitatively reproduce the measured mild amplitude decay up to $x/x_{MIZ} < 0.6$ followed by a sharp decline (see figure 2*c*). Other models, i.e. the exponential and non-drifting models, better reproduce the attenuation near to the ice edge, but fail to capture the sharp decline deeper into the sea ice. The predictive performance of the drifting model is clearly highlighted by the attenuation rate, shown in figure 2(*d*), where the steady attenuation rate near the ice edge followed by rapid growth for $x/x_{MIZ} > 0.6$ are well captured qualitatively and quantitatively. Note that the observed attenuation rate fluctuates, resulting in negative values close to the edge and again at $x/x_{MIZ} \approx 0.4$, and the models cannot capture this behaviour. A jump discontinuity appears at $x/x_{MIZ} \approx 0.1$, consistent with the choice of v resulting in $|v|/U_0 \approx 0.9$ and the presence of $\hat{x}^*$ within the domain. Unlike our formulation, all other models predict either a decreasing attenuation rate (no drift model) or constant attenuation (exponential model), as shown in figure 2(*d*).

In summary, transects I and II showcase two different regimes; in transect I drag attenuation is weak ($\delta = 0.6$) whereas in transect II it is the dominant mechanism ($\delta = 8.0$). Therefore, as expected, in transect I deviations from exponential attenuation are weaker than in transect II; however, also in transect II, the inclusion of exponential

attenuation through α provides significantly improved predictions. When drag dominates, the extinction location x_{end} occurs earlier and the spike in attenuation is more prominent.

Our model is developed for homogeneous sea-ice conditions, implying constant C_d along the transect. While this hypothesis is more likely to hold in the winter season (transect II) its applicability to transect I is more debatable. Moreover, direct comparison with individual observations is made difficult by inherent measurement uncertainty, including misalignenment of the transect with the wave direction Voermans *et al.* (2025), lack of information on the local sea-ice properties and the possible presence of other forcing mechanisms in the wave transport equation, e.g. wind forcing. Nevertheless, we highlight that our simple model captures the observed feature of wave attenuation in the MIZ.

3.2. *Averaged attenuation*

Voermans *et al.* (2025) report average attenuation profiles across seasons and sectors of the Antarctic MIZ. To reproduce the observed variability, we drive our model, i.e. (2.15), with $N_0 = 3 \times 10^5$ random realisations with Gaussian distributed drift velocity (with mean μ_v and standard deviation σ_v), constant throughout the transect. Each realisation corresponds to an individual transect and N denotes the number of transects at any given location according to our model, the decrease is due to individual transects reaching the extinction location. The simulations replicate the variability of drift around Antarctica (Kwok *et al.* 2017). The attenuation rate is computed for the wave component $T = 12$ s (angular frequency $\Omega = 0.52\ \mathrm{s}^{-1}$ and wavelength $\lambda = 225$ m) and we set the wave amplitude at the sea-ice edge to $a_0 = 1$ m. The other parameters are $C_d = 0.02$ and $\alpha = 7.0 \times 10^{-6}\ \mathrm{m}^{-1}$, to match the averaged measured attenuation rate at the sea-ice edge. While the drag coefficient is higher than the one chosen for the individual transects in the previous section, its value is within the range of observed values for the MIZ (McPhee 1979). Moreover, the chosen value allows us to quantitatively match the observed attenuation rate close to the sea-ice edge, as reported in Voermans *et al.* (2025). Smaller values of drag would give rise to a similar qualitative behaviour. For the comparison, only $a \geqslant 0.05$m are averaged, in accordance with the methodology used by Voermans *et al.* (2025) to exclude observations with high uncertainty.

For drift $\mu_v = 0.22\ \mathrm{m\,s}^{-1}$ ($\mu_v/U_0 = 0.42$) and standard deviation $\sigma_v = 0.03\ \mathrm{m\,s}^{-1}$ (figure 3*a*) the attenuation only slightly increases up to $x/\lambda \approx 550$, consistent with the fact that simulations are in weak drag regime ($\delta = 0.42$). From $x/\lambda \approx 550$ to $x/\lambda \approx 700$ the increase is more noticeable, up to ≈ 3 times the attenuation rate at the sea-ice edge, in qualitative agreement with simulations for transect I (cf. figure 2*b*), before stabilising farther in the sea-ice domain. The spread of individual profiles, shaded in grey, also grows when the attenuation rate increases. Note that the increase in attenuation corresponds to a reduction in available measurements of amplitude over threshold (shown in red) and, similarly, individual amplitude profiles reaching the extinction location (distribution shaded in blue).

With the same average drift ($\mu_v = 0.22$ m s^{-1}) but lower variability (from $\sigma_v = 0.03$ m s^{-1} to $\sigma_v = 0.01$ m s^{-1}; figure 3*b*) the same qualitative behaviour is observed. The increase in attenuation is sharper, i.e. it starts deeper in the sea ice (at $\approx$650 wavelengths) and reaches higher values ($\alpha_{eff} \approx 5.5 \times 10^{-4}$ vs $\alpha_{eff} \approx 3.5 \times 10^{-4}$).

The increase in drift ($\mu_v = 0.29$ m s^{-1}, $\mu_v/U_0 = 0.55$ and $\sigma_v = 0.03$ m s^{-1}; figure 3*c*) results in higher $\delta = 0.55$, still in the weak drag regime, and moves the increase in attenuation rate closer to the sea-ice edge, from $x/\lambda \approx 450$ to $x/\lambda \approx 550$. A slightly higher

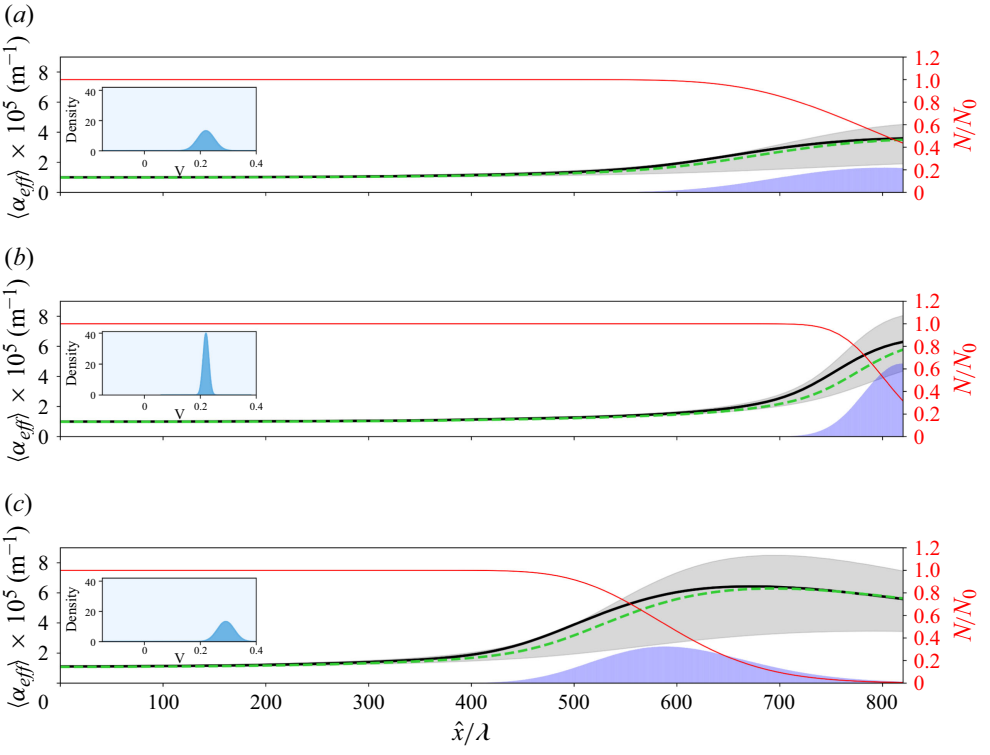

Figure 3. Averaged attenuation rates (in black; for negative velocity in green) and interquartile range (shaded in grey). On the right axis, number of measurements (in red) and distribution of the extinction location (shaded in blue; not to scale). Insets show the corresponding drift velocity distribution: (*a*) $\mu_v = 0.22$ m s^{-1} $\sigma_v = 0.03$ m s^{-1}; (*b*) $\mu_v = 0.22$ m s^{-1} $\sigma_v = 0.01$ m s^{-1}; (*c*) $\mu_v = 0.29$ m s^{-1} $\sigma_v = 0.03$ m s^{-1}.

attenuation is also achieved compared with the previous cases, up to $\alpha_{eff} \approx 6 \times 10^{-4}$, after which it decreases slightly. For smaller drag coefficients results the increase in attenuation occurs further into the ice field. The number of observations decreases sharply due to individual transects reaching their extinction location (cf. figure 1*b*), and only less than 0.1 % remain after 800 wavelengths, also explaining the larger variance in effective attenuation.

In figure 3 the mean attenuation rates for negative mean velocity are also reported in the dashed green line. The direction of the drift has only a marginal effect on the effective attenuation profile, i.e. the growth of the attenuation rate is deeper into the sea ice (by ≈10 wavelengths) but does not affect its magnitude, with a similar effect on the available measurements and extinction location distributions. This is expected for oceanic conditions, as $\alpha \approx \alpha_{exp}$ and $\Gamma \approx C_d/(g c_g 2\pi)$, hence the dependence of direction of the drift is negligible for operational purposes.

Figure 3(*c*) is remarkably similar to the measured averaged attenuation in Voermans *et al.* (2025), i.e. a linear increase followed by slight decline, also matching the range of observed attenuation rates. Unlike in the measurements, in the model all individual transects are available from the edge but the decrease of available observations in Voermans *et al.* (2025) deeper into the sea ice is also captured. It can be argued that the presence of drift limits the extent of the wave-affected area, and its extent in our model (≈ 185 km; figure 3(*c*)) is consistent with a MIZ width of the order of 200 km, as reported in observations (Brouwer *et al.* 2022) and model simulations (Day *et al.* 2024).

4. Conclusions

We derived a mechanistic model for wave attenuation that accounts for both phenomenological exponential attenuation mechanisms and dissipation due to drag at the ocean–sea-ice interface, as well as the effect of sea-ice drift, therefore combining and extending previous models in which drift was excluded (cf. Shen & Squire 1998; Kohout *et al.* 2011; Herman *et al.* 2019). We identified the parameter δ which governs attenuation dominated by drift-induced drag mechanisms ($\delta > 1$) and exponential mechanisms ($\delta < 1$). Analytical solutions reveal that in the drift-induced drag dominated regime, the amplitude eventually dies off, unlike prediction based on exponential attenuation, and the attenuation profile spikes close to the extinction location.

The model agrees well, both qualitatively and quantitatively, with pan-Antarctic measurements of attenuation rate recently reported by Voermans *et al.* (2025) when sea ice is allowed to drift slowly ($\mu_v / U_0 = 0.55$), even for small δ, i.e. $\delta = 0.55$. In particular, drift is responsible for the increase in the wave attenuation rate deeper into the sea ice and, to a certain extent, regulates the width of the wave-affected sea ice which is in quantitative agreement to the MIZ extent (100–200 km) reported for observations (Brouwer *et al.* 2022) and model simulations (Day *et al.* 2024).

The quantitative agreement against individual transects is reasonable, with limitations. Differences from the measured observations can be attributed to experimental uncertainty and current model assumptions, i.e. no interaction between wave components, no presence of other forcing mechanisms, homogeneous drift and sea-ice properties along the transect. Some of the limitations of the model could be sought by seeking numerical solutions for the governing equation, (2.5), and allowing for spatially heterogenous parameters. In this regard, our modelling framework allows for easy implementation into operational models and the biggest limitation, common to many wave attenuation models, is the lack of physically informed sea-ice parameters along the MIZ.

Ultimately the model provides a solid theoretical foundation to better interpret observations of wave attenuation in drifting sea ice as found around Antarctica, and prompts new concurrent measurements of waves, drift and sea-ice properties for further validation. Moreover, while only drag has been studied explicitly, the approach can be extended to better specify other wave attenuation mechanisms for integration in emerging coupled ocean–wave–sea-ice models such as the ones currently being developed in most weather forecasting agencies (Kousal *et al.* 2026), e.g. the European Centre for Medium-Range Weather Forecasts.

Acknowledgements. This work was supported by the Natural Environment Research Council and the ARIES Doctoral Training Partnership [grant number NE/S007334/1]. R.R. and A.A. acknowledge funding from Royal Society (IEC\R3\243016). This work was stimulated by discussions during the 'Maths of Sea Ice' meeting, made possible by the Isaac Newton Institute for Mathematical Sciences. D.P. is supported by EPSRC Grant No. EP/Y021118/1 and by the ExtreMe Matter Institute EMMI at the GSI Helmholtzzentrum fuer Schwerionenphysik, Darmstadt, Germany.

Declaration of interests. The authors report no conflicts of interest.

Appendix A. Integral approximation

The integral I in (2.7)

$$I = \int_0^{2\pi} |U \sin\phi - v|^3 \, \mathrm{d}\phi, \tag{A.1}$$

is treated differently for $|v| \ll a\Omega$ (or equivalently $|v| \ll U$) and $|v| > a\Omega$ (or equivalently $|v| > U$).

A.1. *Case* $|v| \ll U$.

We expand the integrand as

$$|U\sin\phi - v|^3 = |U\sin\phi|^3 - 3vU^2\sin^2\phi\,\mathrm{sgn}(\sin\phi)\sin\phi + 3v^2U|\sin\phi| + O\big(v^3\big). \tag{A.2}$$

The second term makes zero contribution towards I. Therefore, we approximate the integral as a polynomial in U

$$I \approx \int_0^{2\pi} \Big(U^3|\sin\phi|^3 + 3Uv^2|\sin\phi|\Big)\,\mathrm{d}\phi = \frac{8}{3}U^3 + 12Uv^2. \tag{A.3}$$

While strictly valid only for $|v| \ll U$ we use this approximation for $|v| \leqslant U$.

A.2. *Case:* $|v| > U$

The integrand only depends on the sign of v. Therefore it can be written as

$$|U\sin\phi - v|^3 = \mathrm{sign}(v)\,(v - U\sin\phi)^3. \tag{A.4}$$

Note that some of the terms make zero contribution towards I due to symmetry. We write the integral as a polynomial

$$I = \int_0^{2\pi} \Big(|v|^3 + 3|v|U^2\sin^2\phi\Big)\,\mathrm{d}\phi, \tag{A.5}$$

$$I = 2\pi|v|^3 + 3\pi U^2|v|. \tag{A.6}$$

Appendix B. Analytical solutions

The integral approximation I is piecewise, i.e. depends on the relationship between U and v. As a result, different governing equations emerge for solutions in region A, corresponding to $a\Omega \geqslant |v|$, and region B for $a\Omega < |v|$. We first solve the governing equation for a in region A and then impose continuity on the amplitude to obtain the solution in region B.

B.1. *Region A*

In region A, defined as the region in which orbital velocity is greater than the drift ($a\Omega \geqslant |v|$), if it exists we impose the initial condition $a(\hat{x} = 0) = a_0$.

The governing equation in its differential and integral form is

$$\frac{\mathrm{d}a_A}{\mathrm{d}\hat{x}} = -\alpha a_A - \frac{8}{3}\Gamma\Omega^3 a_A^2 - 12\Gamma\Omega|v|^2 \equiv -f(a), \tag{B.1}$$

$$\int_{a_0}^{a_A} \frac{\mathrm{d}a'}{\frac{8}{3}\Gamma\Omega^3 a'^2 + \alpha a' + 12\Gamma\Omega|v|^2} = -\hat{x}. \tag{B.2}$$

The sign of the discriminant of f, denoted as Δ, sets the form of solution.

The roots of f are $r_\pm$.

The solutions are categorised according to Δ

$$a_A(\hat{x}) = \begin{cases} \dfrac{3\sqrt{\Delta}}{16\Gamma\Omega^3}\tan\left(-\dfrac{\sqrt{\Delta}}{2}\hat{x} + \arctan\left(\dfrac{16\Gamma\Omega^3 a_0 + 3\alpha}{3\sqrt{\Delta}}\right)\right) - \dfrac{3\alpha}{16\Gamma\Omega^3}, & \Delta > 0, \\ \dfrac{32\Gamma\Omega^3 a_0 - \left(16\alpha\Gamma\Omega^3 a_0 + 3\alpha^2\right)\hat{x}}{32\Gamma\Omega^3 + \left(32\Gamma\Omega^3 a_0 + 6\alpha\right)\hat{x}}, & \Delta = 0, \\ \dfrac{r_-(a_0 - r_+)\exp\left(\dfrac{8\Gamma\Omega^3}{3}(r_- - r_+)\hat{x}\right) - r_+(a_0 - r_-)}{(a_0 - r_+)\exp\left(\dfrac{8\Gamma\Omega^3}{3}(r_- - r_+)\hat{x}\right) - (a_0 - r_-)}, & \Delta < 0. \end{cases} \tag{B.3}$$

Because the relationship between Δ and δ, we can rewrite the condition as function of δ as in (2.9).

We define $\hat{x}^*$ as the location where $U(\hat{x}^*) = |v|$, or equivalently $a(\hat{x}^*)\Omega = |v|$. Therefore

$$\hat{x}^* = \max\left\{ a^{-1}\left(\frac{|v|}{\Omega}\right),\ 0 \right\}, \tag{B.4}$$

denotes the extent of region A.

B.2. *Region B*

In region B we enforce continuity of the amplitude at $\hat{x}^*$. Note that if the orbital velocity at the ice edge is lower that the drift, only region B exists. Using the integral approximation, the differential and integral forms of the governing equation are

$$\frac{\mathrm{d}a_B}{\mathrm{d}\hat{x}} = -\left(\alpha + 3\pi\Gamma\Omega^2|v|\right)a_B - \frac{2\pi\Gamma|v|^3}{a_B}, \tag{B.5}$$

$$\int_{a_A(x^*)}^{a_B} \frac{a'}{\left(\alpha + 3\pi\Gamma\Omega^2|v|\right)a'^2 + 2\pi\Gamma|v|^3}\,\mathrm{d}a' = x^* - \hat{x}. \tag{B.6}$$

The integrand yields

$$a_B(\hat{x}) = \left[e^{-(6\pi\Omega^2|v|\Gamma + 2\alpha)(\hat{x} - \hat{x}^*)}\left(\frac{v^2}{\Omega^2} + \frac{2\pi|v|^3\Gamma}{3\pi\Omega^2|v|\Gamma + \alpha}\right) - \frac{2\pi|v|^3\Gamma}{3\pi\Omega^2|v|\Gamma + \alpha}\right]^{\frac{1}{2}}, \quad \hat{x} \geqslant \hat{x}^*. \tag{B.7}$$

References

Alberello, A., Bennetts, L., Heil, P., Eayrs, C., Vichi, M., MacHutchon, K., Onorato, M. & Toffoli, A. 2020 Drift of pancake ice floes in the winter antarctic marginal ice zone during polar cyclones. *J. Geophys. Res.: Oceans* **125** (3), e2019JC015418.

Alberello, A., *et al.* 2022 Three-dimensional imaging of waves and floes in the marginal ice zone during a cyclone. *Nat. Commun.* **13** (1), 1–11.

Alberello, A., Onorato, M., Bennetts, L., Vichi, M., Eayrs, C., MacHutchon, K. & Toffoli, A. 2019 Brief communication: pancake ice floe size distribution during the winter expansion of the Antarctic marginal ice zone. *Cryosphere* **13** (1), 41–48.

Barrell, C., *et al.* 2025 Rapid summertime sea ice melt in a coupled numerical weather prediction system. *J. Adv. Model. Earth Syst.* **17** (10), e2025MS004945.

Bennetts, L.G., *et al.* 2024 Closing the loops on Southern Ocean dynamics: from the circumpolar current to ice shelves and from bottom mixing to surface waves. *Rev. Geophys.* **62** (3), e2022RG000781.

BROUWER, J., *et al.* 2022 Altimetric observation of wave attenuation through the antarctic marginal ice zone using ICESat-2. *Cryosphere* **16** (6), 2325–2353.

DAY, J., KEELEY, S., ARDUINI, G., MAGNUSSON, L., MOGENSEN, K., RODWELL, M., SANDU, I. & TIETSCHE, S. 2022 Benefits and challenges of dynamic sea-ice for weather forecasts. *Weather Climate Dyn. Discuss* **2022**, 1–28.

DAY, N.S., BENNETTS, L.G., O'FARRELL, S.P., ALBERELLO, A. & MONTIEL, F. 2024 Analysis of the Antarctic marginal ice zone based on unsupervised classification of standalone sea ice model data. *J. Geophys. Res.: Oceans* **129** (8), e2024JC020953.

DERKANI, M.H., ALBERELLO, A., NELLI, F., BENNETTS, L.G., HESSNER, K.G., MACHUTCHON, K., REICHERT, K., AOUF, L., KHAN, S.S. & TOFFOLI, A. 2020 Wind, waves, and surface currents in the Southern Ocean: observations from the Antarctic Circumnavigation Expedition. *Earth Syst. Sci. Data Discuss.* **2020**, 1–22.

ELVIDGE, A.D., RENFREW, I.A., WEISS, A.I., BROOKS, I.M., LACHLAN-COPE, T.A. & KING, J.C. 2016 Observations of surface momentum exchange over the marginal ice zone and recommendations for its parametrisation. *Atmos. Chem. Phys.* **16** (3), 1545–1563.

FOX, C. & SQUIRE, V.A. 1994 On the oblique reflexion and transmission of ocean waves at shore fast sea ice. *Phil. Trans. R. Soc. Lond. A* **347** (1682), 185–218.

HERMAN, A., CHENG, S. & SHEN, H.H. 2019 Wave energy attenuation in fields of colliding ice floes – Part 1: Discrete-element modelling of dissipation due to ice–water drag. *Cryosphere* **13** (11), 2887–2900.

HOLLAND, P.R. & KWOK, R. 2012 Wind-driven trends in Antarctic sea-ice drift. *Nat. Geosci.* **5** (12), 872–875.

IPCC 2021 *Climate Change 2021: The Physical Science Basis. Contribution of Working Group I to the Sixth Assessment Report of the Intergovernmental Panel on Climate Change*. Cambridge University Press.

KELLER, J.B. 1998 Gravity waves on ice-covered water. *J. Geophys. Res.: Oceans* **103** (C4), 7663–7669.

KOHOUT, A.L., MEYLAN, M.H. & PLEW, D.R. 2011 Wave attenuation in a marginal ice zone due to the bottom roughness of ice floes. *Ann. Glaciol.* **52** (57), 118–122.

KOHOUT, A.L., SMITH, M., ROACH, L.A., WILLIAMS, G., MONTIEL, F. & WILLIAMS, M.J.M. 2020 Observations of exponential wave attenuation in Antarctic sea ice during the PIPERS campaign. *Ann. Glaciol.* **61** (82), 196–209.

KOHOUT, A.L., WILLIAMS, M.J.M., DEAN, S.M. & MEYLAN, M.H. 2014 Storm-induced sea-ice breakup and the implications for ice extent. *Nature* **509** (7502), 604–607.

KOUSAL, J., *et al.* Xabier Pedruzo 2026 Numerical weather prediction model coupling—strategies, challenges, and outlook. *B. Am. Meteorol. Soc.* **107** (1), E183–E189.

KWOK, R., PANG, S.S. & KACIMI, S. 2017 Sea ice drift in the Southern Ocean: regional patterns, variability, and trends. *Elementa* **5**, 32.

SCHMALE, J. 2021 Exploring the coupled ocean and atmosphere system with a data science approach applied to observations from the Antarctic Circumnavigation Expedition. *Earth Syst. Dyn* **12** (4), 1295–1369.

MCPHEE, M.G. 1979 The effect of the oceanic boundary layer on the mean drift of pack ice: application of a simple model. *J. Phys. Oceanogr.* **9** (2), 388–400.

MEYLAN, M.H., BENNETTS, L.G., MOSIG, J.E.M., ROGERS, W.E., DOBLE, M.J. & PETER, M.A. 2018 Dispersion relations, power laws, and energy loss for waves in the marginal ice zone. *J. Geophys. Res.: Oceans* **123** (5), 3322–3335.

MONTIEL, F., FORBES, M., ECHEVARRIA, E., RAPIZO, H. & GAMBLE, C. 2025 Evaluation of ice dissipation parameterizations in spectral ocean wave model WAVEWATCH III: an intercomparison analysis. *J. Geophys. Res.: Oceans* **130** (9), e2024JC022113.

MONTIEL, F., KOHOUT, A.L. & ROACH, L.A. 2022 Physical drivers of ocean wave attenuation in the marginal ice zone. *J. Phys. Oceanogr.* **52** (5), 889–906.

ROBINSON, N.J. & PALMER, S.C. 1990 A modal analysis of a rectangular plate floating on an incompressible liquid. *J. Sound Vib.* **142** (3), 453–460.

SELIVANOVA, J., IOVINO, D. & COCETTA, F. 2024 Past and future of the Arctic sea ice in high-resolution model intercomparison project (HighResMIP) climate models. *Cryosphere* **18** (6), 2739–2763.

SHEN, H.H. & SQUIRE, V.A. 1998 Wave damping in compact pancake ice fields due to interactions between pancakes. *Antarctic Sea Ice: Phys. Processes Interactions and Variability* **74**, 325–341.

SMITH, M. & THOMSON, J. 2020 Pancake sea ice kinematics and dynamics using shipboard stereo video. *Ann. Glaciol.* **61** (82), 1–11.

STOPA, J.E., SUTHERLAND, P. & ARDHUIN, F. 2018 Strong and highly variable push of ocean waves on Southern Ocean sea ice. *Proc. Natl Acad. Sci.* **115** (23), 5861–5865.

VICHI, M. 2022 An indicator of sea ice variability for the Antarctic marginal ice zone. *Cryosphere* **16** (10), 4087–4106.

VICHI, M., *et al.* 2019 Effects of an explosive polar cyclone crossing the antarctic marginal ice zone. *Geophys. Res. Lett.* **46** (11), 5948–5958.

VOERMANS, J.J., FRASER, A.D., BROUWER, J., MEYLAN, M.H., LIU, Q. & BABANIN, A.V. 2025 Finely resolved along-track wave attenuation estimates in the Antarctic marginal ice zone from ICESat-2. *Cryosphere* **19** (8), 3381–3395.

WADHAMS, P. 1978 Wave decay in the marginal ice zone measured from a submarine. *Deep Sea Res.* **25** (1), 23–40.

WADHAMS, P. 1986 *The Seasonal Ice Zone*, pp. 825–991. Springer US.

WAMSER, C. & MARTINSON, D.G. 1993 Drag coefficients for winter Antarctic pack ice. *J. Geophys. Res.: Oceans* **98** (C7), 12431–12437.

WANG, R. & SHEN, H.H. 2010 Gravity waves propagating into an ice-covered ocean: a viscoelastic model. *J. Geophys. Res.: Oceans* **115** (C6). Available at: https://agupubs.onlinelibrary.wiley.com/doi/full/10.1029/2009JC005591.

WEBER, J.E. 1987 Wave attenuation and wave drift in the marginal ice zone. *J. Phys. Oceanogr.* **17** (12), 2351–2361.

WOMACK, A., ALBERELLO, A., DE, V., MARC, T., ALESSANDRO, V., Robyn, & VICHI, M. 2024 A contrast in sea ice drift and deformation between winter and spring of 2019 in the antarctic marginal ice zone. *Cryosphere* **18** (1), 205–229.

WOMACK, A., VICHI, M., ALBERELLO, A. & TOFFOLI, A. 2022 Atmospheric drivers of a winter-to-spring lagrangian sea-ice drift in the eastern antarctic marginal ice zone. *J. Glaciol.* **68** (271), 999–1013.